Available online at www.sciencedirect.com
SCIENCE DIRECT
Journal of Magnetic Resonance 178 (2006) 308–317
JMR Journal of Magnetic Resonance
www.elsevier.com/locate/jmr

Application of **k**- and **q**-space encoding NMR techniques on granular media in a 3D model fluidized bed reactor

Silke Harms, Siegfried Stapf *, Bernhard Blümich

Institute (formerly Instituet) of Technical Chemistry and Macromolecular Chemistry, ITMC, RWTH Aachen, Worringer Weg 1, 52074 Aachen, Germany

Received 18 July 2005; revised 17 October 2005
Available online 2 November 2005

Abstract

A combination of PFG–NMR imaging and velocity encoding methods was applied to investigate the dynamic behavior of a bed of poppy seeds subjected to air flow, representing a model setup for fluidized bed reactors. The particle motion is described both from a statistical point of view, by determining propagators and dispersion coefficients representing an average over the whole bed volume, as well as combined with spatial resolution by generating velocity maps. Velocity images of different horizontal slices in the bed confirm the notion of a toroidal particle flow pattern inside the shallow granular bed. Despite the need of considerable averaging due to the random motion of the relatively few particles in the bed, quantitative velocity images and statistical information about the random particle motion can be obtained from monitoring the fluid component in the seeds by conventional spin-echo techniques.

Keywords: Granular flow; PGSTE NMR; Propagator; Dispersion coefficient; Velocity imaging

1. Introduction

1.1. Granular media

Granular materials constitute a class of systems of widespread interest. They appear in a huge range of production processes and are also important in conjunction with natural phenomena like sedimentation and avalanches. Considering the analogy between molecules and macroscopic particles, they bear a certain similarity to real fluids but their collective behavior cannot be described in terms of Brownian motion [1].

Granular media, in general, are often understood as sets of particles of sufficient size so that thermal fluctuations become of negligible importance. In comparison to molecules, the interactions are different because of the role of energy dissipation due to collisions. In the case of granular media, inelastic impacts and friction result in an energy loss unlike in fluids. For an overview about the properties and the physical background of granular media, we refer the reader to standard textbooks [1,2]. One straightforward approach has been to classify granular materials in terms of size, which is followed by Brown and Richards [3]. In their classification, broken solids, granular solids, and different types of powders are distinguished. The classification system developed by Geldart [4] focuses on the dynamic behavior and relates to the special situation of fluidized systems (see following section).

Experimental techniques that have been used for investigating granular media predominantly rely on optical methods, despite the fact that the systems of interest are frequently opaque and only the outer region of the granular bed becomes directly accessible. Other radiation-based techniques (infra-red light, X-rays, and γ-rays) were applied to avoid this problem, but also electrical methods such as the measurement of capacitance, conductance or impedance, and methods based on mechanical properties such as ultrasound, absolute pressure, or differential pressure were applied (see [2,5]).

Magnetic Resonance Imaging methods were applied to granular media in various contexts like mixing, segrega-

* Corresponding author. Fax: +49 241 80 22185.
E-mail address: sstapf@mc.rwth-aachen.de (S. Stapf).

1090-7807/$ - see front matter © 2005 Elsevier Inc. All rights reserved.
doi:10.1016/j.jmr.2005.10.009

tion, and flow phenomena. Miscellaneous systems and geometries are under study: segregation and flow of granular media in rotating cylinders were investigated by several researchers [6–10], whereas Yamane et al. [8] compared the results of the MRI measurements with discrete element method simulations. Mueth studied particle dynamics in a 3D Couette cell [11], while Porion et al. [12] measured the mixing process in a 3D blender by MRI. The conditions of vibrofluidized beds were investigated by several groups [13–20]. For a complete survey on MRI on granular materials, the reader is referred to [21,22].

1.2. Fluidized beds

Among the different possibilities to induce motion in granular systems, fluidization processes are a particularly important class of procedures that see widespread applications in the technical and chemical engineering industry [23]. Probably the most relevant realization is found in fluidized bed reactors which are being used in, for instance, coal combustion, drying, heat exchange or catalytic reactions that depend on good contact between the gas phase and the catalytic sites as well as easy replacement of the catalyst carrier. The fluidized bed reactor was developed as a coal combustion process in 1922 by Winkler at BASF (DRP 437 970). In general, a fluidized bed describes the realization of aerating a solid packing via a gas (or liquid) stream against gravitational forces. More than 500 patents were applied considering fluidized beds in a period of 10 years (1946–1956) [24] because of its straightforward evolution in many industrial processes. The different behavior of particles subjected to the streaming continuous phase has led Geldart to establish a classification scheme of granular media based on their dynamic behavior. His scheme of four groups (A–D) considers, apart from the fluidization ability, the size or bulk density of the particles, the expansion of the packing, the gas velocity in between the packing, and the velocity of the rising gas bubbles. Because of the wide diversity of phenomena found in this two-phase system of solids and gas, and the mutual dependence of the motions of both phases, experimental techniques have been used, that access either of the two phases and deduce information about the complementary one, an approach outlined in [25]. Early investigations of gas-fluidized beds include Werther's electrical techniques with the aim to obtain insight into the fluid mechanics and the growth and size distribution of bubbles rising inside the fluidized bed [26,27]. Also optical methods on 2D models of the fluidized bed were employed [28]. Much more recently, Valverde et al. [29] used ultrasonic techniques to study the effect of particle size and interparticle force, and they studied diffusive processes of small particles from a statistical point of view [30]. Measurements using diffusing-wave spectroscopy were performed by Menon and Durian [31] to study particle motion inside fluidized beds. At the same time, experimental results were supported by numerical simulations that focused on different aspects of the behavior of such a particle system [32–35].

The potential of MRI to visualize velocity patterns inside gas-fluidized beds directly has, however, not yet been exploited, contrary to the works on vibrofluidized beds mentioned above [13–20]. Just like in any investigation of granular media by NMR methods, the possibilities to extract spatial information about the particles is compromised by the need to have a signal of sufficient lifetime to allow imaging or the encoding of motional parameters. Fennell et al. [36] have circumvented the problem by fast imaging of the mixing process of NMR-visible and -invisible solids in gas-fluidized packings. Exchange and velocity distributions in the gas phase have been the subject of the studies of Wang et al. [37], who used ^{129}Xe NMR of xenon-containing gas stream in a fluidized bed. In [38] bed densities and velocity distributions of fluidized particles were obtained in a model reactor geometry, but the direct visualization of motion patterns by combination with MRI has not been reported yet.

This work aims at measuring and visualizing the particle motion in a shallow, narrow-bore gas-fluidized granular bed. In dependence of the gas flow rate, the ideal bed can be found in any of four different stages that are used to characterize the dynamic state of a granular bed; for small flow rates, the system is in the fixed phase, where the particles rest on the bottom (Fig. 1A). If the flow rate is increased above a critical value, the particles begin to move and reach the homogeneous fluidized phase, which is characterized by a slight decrease in density and a mobile surface that resembles liquid-like behavior. With further increase of the flow rate, the so-called bubbling phase is observed, where gas bubbles travel upward through the medium, carrying solid particles with them; the bubbles are not fully reproducible, and the local density and motion in the system can only be defined in a time-averaged fashion (Fig. 1C). Werther [26,27] observed the motion of particles and bubbles also in dependence of the diameter of the reactor, which is an important issue for scale-up towards industrial applications, where diameters of several meters are not uncommon. His findings were that smaller reactors

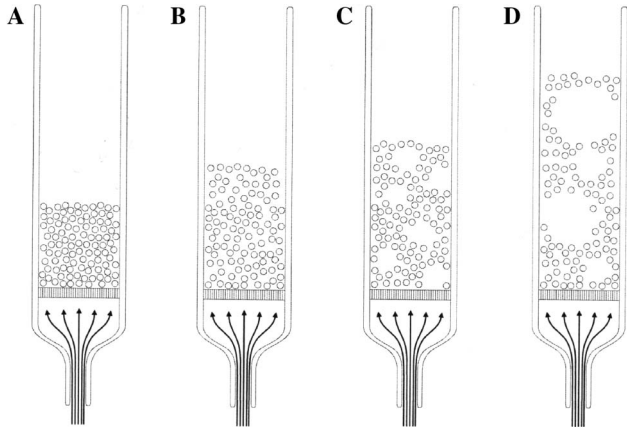

Fig. 1. States of a fluidized bed, according to [41,42]: (A) fixed phase; (B) homogeneous fluidized phase; (C) bubbling phase; and (D) slugging phase.

with diameters below 200 mm and those with a large height to diameter ratio [27] are affected by the undesired slugging phase; for bubbles above a certain size, coalescence can lead to the formation of a slugging phase, where gas volumes with a diameter equal to that of the column are moving upwards, hereby transporting particles out of the column (see Fig. 1D). In this context Werther presented a scheme of the movement of both bubbles and particles for smaller bed widths (Fig. 2A). Whereas the bubbles rise from the bottom and disappear while leaving the bed (non-vanishing net transport of *gas* through the bed), the particles are first transported upward with the gas phase but then fall, like in a spout, to the inner wall and move downwards to the ground, where the cycle starts again (vanishing net transport of *solids*). The pattern of particle motion is drawn in a simplified manner in Fig. 2B. In Fig. 2C, the coordinate frame for the following NMR experiments is drawn. Despite the fact that a single circulation cell is commonly described in the literature, multiple cells have actually been reported [39,40] so that a verification of the pattern shown in Figs. 2A and B is indeed desirable.

The materials which were investigated in this paper belong to Geldart group D. This group is defined by relatively large and heavy particles, and the velocity of the gas streaming through the packed particles is higher than the velocity of the rising gas bubbles [4]. The homogeneous fluidized state (Fig. 1B) is relatively difficult to realize with particles of the Geldart group D, a fact that has been reported earlier [4,42,44]. Rather than discussing the homogeneous phase, this work concentrates on a qualitative understanding of the flow patterns in the bubbling phase, which is also of much higher technical importance. Fluidized beds with small height to diameter ratios are defined by the appearance of typically more than one "circulation cell" [27], in case of large bed diameters and, in comparison, small particle size. The system under study does have a small height to diameter ratio but rather large particles which also affects the fluidization behaviour. In the presented case, one would therefore expect a single circulation cell. The purpose of this work is to demonstrate the feasibility and limitations of particle velocity measurements by PFG–NMR, and to compare the experimental results with these qualitative model descriptions.

2. Theoretical background

The propagator [45] describes the probability density of displacements, and therefore also of velocities (velocity distribution). It is obtained by conventional PGSE (Pulsed Gradient Spin Echo) experiments [46]. The sequence used in this work consists of a basic stimulated-echo experiment with an additional pair of bipolar gradients after the first and the third 90° pulses. The two gradient pulses have duration δ and separation Δ, where Δ is equivalent to the velocity encoding time. The detected signal after **q**-space encoding has the form $S(\mathbf{q},\Delta)$:

$$S(\mathbf{q},\Delta) = \int\int \rho(\mathbf{r})P(\mathbf{r}|\mathbf{r}',\Delta)\exp\{i2\pi\mathbf{q}(\mathbf{r}-\mathbf{r}')\}\,d\mathbf{r}'\,d\mathbf{r}, \quad (1)$$

which, by replacing $\mathbf{r}' = \mathbf{r} + \mathbf{R}$, can be written as:

$$S(\mathbf{q},\Delta) = \int \overline{P}(\mathbf{R},\Delta)\exp(i2\pi\mathbf{q}\cdot\mathbf{R})\,d\mathbf{R}. \quad (2)$$

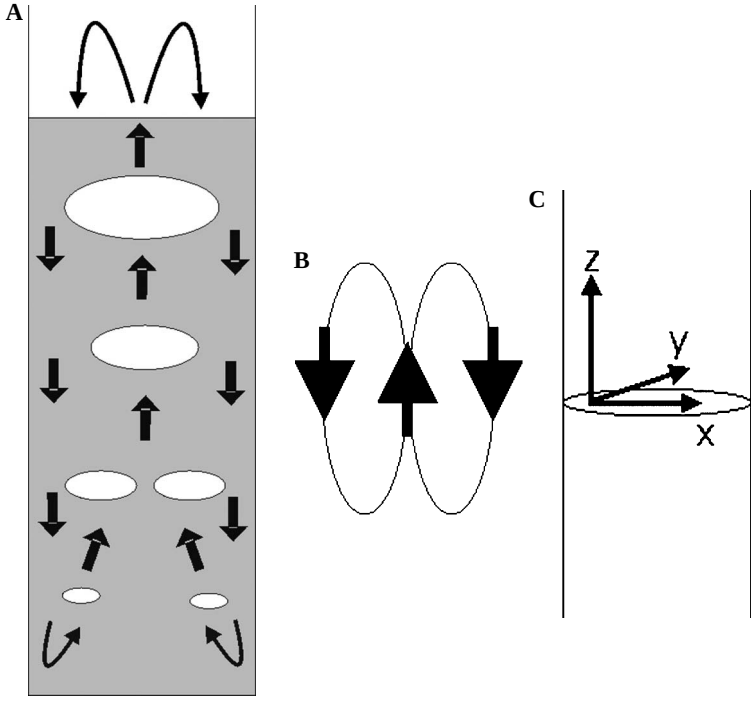

Fig. 2. (A) Particle circulation in fluidized beds [27,43]; (B) simplified model; and (C) definition of the coordinate frame.

Here, **R** is the displacement during the interval Δ. The propagator $\overline{P}(\mathbf{R},t)$ describes the average probability for every particle of accumulating a displacement **R** during the interval t [42], averaged over the starting position **r**:

$$\overline{P}(\mathbf{R},t) = \int P(\mathbf{r}|\mathbf{r}+\mathbf{R},t)\rho(\mathbf{r})\,\mathrm{d}\mathbf{r}, \tag{3}$$

where $P(\mathbf{r}|\mathbf{r}+\mathbf{R},t)$ is the conditional probability of finding a displacement **R** *given that* the initial position has been **r**. In case of free self-diffusion, the term $P(\mathbf{r}|\mathbf{r}+\mathbf{R},t)$ is independent of the initial position of the spins and the average propagator is the same for all spins. One can then write [47]:

$$P(\mathbf{R},t) = (4\pi\cdot Dt)^{-\frac{3}{2}}\exp\left(-\frac{\mathbf{R}^2}{4Dt}\right), \tag{4}$$

where D denotes the self-diffusion coefficient. In the more general case of dispersive motion where an average, non-zero average velocity $\bar{v}$ is present, one obtains:

$$P(\mathbf{R},t) = (4\pi\cdot D_{\mathrm{eff}}t)^{-\frac{3}{2}}\exp\left(-\frac{(\mathbf{R}-\bar{v}t)^2}{4D_{\mathrm{eff}}t}\right). \tag{5}$$

The diffusion coefficient is now replaced by the dispersion coefficient, D_{eff}. In real granular systems, neither of the two conditions—Gaussian statistics nor free motion—is fulfilled. For instance, the model by Werther suggests that velocity distributions need to be dependent on the position inside the bed, and hence the initial position, so that the propagator indeed represents an average taken over particles of different properties. In case of non-Gaussian propagators, the dispersion coefficient can still be obtained from the initial decay of the **q**-space data according to [7]:

$$D(\Delta) \approx -(4\pi^2\Delta)^{-1}\lim_{q\to 0}\frac{\partial\ln|S(\mathbf{q},\Delta)|}{\partial q^2}. \tag{6}$$

In this study, one-dimensional propagators were measured either parallel or perpendicular to the axis of gravity. Dispersion coefficients in both directions were derived using Eq. (6).

To generate velocity encoded images, a simple slice-selective 2D-imaging sequence with an additional pair of gradients was employed. The sequence is shown in Fig. 3,

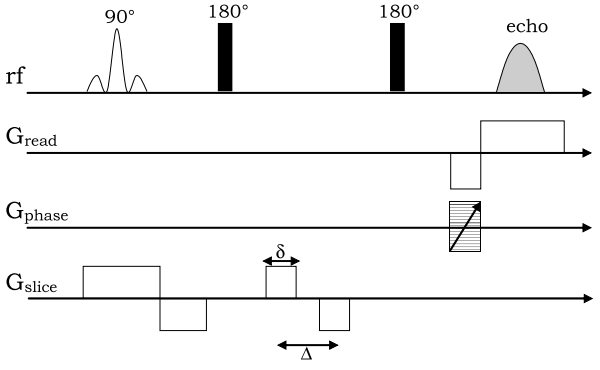

Fig. 3. Two-dimensional velocity encoding imaging sequence, based on a 90°–180°–180° spin-echo-pulse sequence.

where the velocity encoding gradient pair (shown along the slice dimension) can be applied in any of the three spatial directions.

The velocity information is encoded by a standard bipolar gradient pulse pair of pulse duration δ and time separation Δ. It is obtained by analyzing the phase information φ of the complex NMR signal S, Eq. (7).

$$S = S_0\cdot e^{\mathrm{i}\varphi} = S_0(\cos\varphi + \mathrm{i}\sin\varphi),$$
$$\varphi = \arctan\left(\frac{\mathrm{Im}(S)}{\mathrm{Re}(S)}\right). \tag{7}$$

Because φ is obtained through the inverse of tan φ, φ is defined between $-\pi$ and π, and the values of the pulsed gradients have been chosen appropriately to keep the phase angle between these limits. The final images were obtained from two datasets acquired with different values of the velocity encoding gradient, by taking the difference between phases in each pixel, so that spurious phase effects were cancelled out. For generating vector plots, the same procedure has been repeated with velocity gradients being applied in either of two orthogonal directions within a single experiment.

3. Experimental setup

The granular medium under study is a bed of poppy seeds. Following the classification of Duran it is a granular solid, according to Geldart it belongs to group D (see Section 1). The medium was characterized by a sieve analysis, which results in the average particle diameter d_{p} of 880 μm after generating a grading curve. The bulk density ρ_{b} was determined as 663.0 g/L. The ^{1}H relaxation times of the oil inside the seeds, necessary to determine the possible range of encoding and repetition times, were measured as $T_1 = 288$ ms and $T_2 = 85$ ms, respectively, at a Larmor frequency of 200 MHz. The granular medium was filled onto a porous glass frit glued inside a circular glass vessel. The vessel had a length of 100 cm and an inner diameter of 44 mm. To ensure a homogeneous gas flow, the distance from the gas supply to the porous glass plate was 355 mm. Dried air was used as the fluidization gas. The inner diameter of 44 mm was chosen to realize a large cross section to minimize edge effects of particle-wall collisions [26,27,48]. The length of the glass tube avoids particle discharge from the bed.

The measurements were conducted on a BRUKER DSX200 spectrometer controlling a 4.7 T super wide bore magnet. The imaging system was a mini0.36-gradient-system equipped with a ^{1}H 50 mm birdcage resonator.

Propagators (see previous chapter) were measured for three different gas stream rates (30, 60, and 110 hPa). The rates were detected by a pressure difference device, with sensors being located in the gas feed pipe. All measurements were done in the bubbling phase on an ≈2 cm high poppy seed bed. The velocity encoding gradient was varied in 128 steps between −1.132 and +1.132 G/mm. The

encoding time Δ was 14.5 ms, the duration of the gradient pulses 1 ms, and the number of signal accumulations 160.

For the velocity images and the vector plots, a 5 mm slice of the poppy seed bed was excited either in the upper or the lower part of the bed. 128×128 points in each direction and 40 signal averages were acquired. The duration δ of the velocity encoding gradient was 1 ms, and the encoding time between the bipolar gradient lobes, Δ, was 4.2 ms, the maximal gradient strength being 0.025 G/mm. The velocity range of the measurement, the so-called field of flow, was 285.6 mm/s. The imaging experiments were carried out at 70 hPa. The velocity images obtained were noise reduced at the edges and smoothed with a two-point-averaging filter. The data were processed with PV-Wave software, version 8.0 (Visual Numerics, 2003).

4. Results and discussion

4.1. Propagators

The velocity distributions averaged over the whole height of the poppy seed bed are shown in Figs. 4 and 5. The first diagram (Fig. 4) shows the dependence of the velocity distribution on gas stream rate in x-direction, i.e., perpendicular to the flow direction of the gas. The second plot (Fig. 5) shows the dependence in z-direction, i.e., in the direction of the gas stream.

The curves in both diagrams are normalized to unit area so that the probability densities are directly comparable. The bottom part of the probability densities is magnified

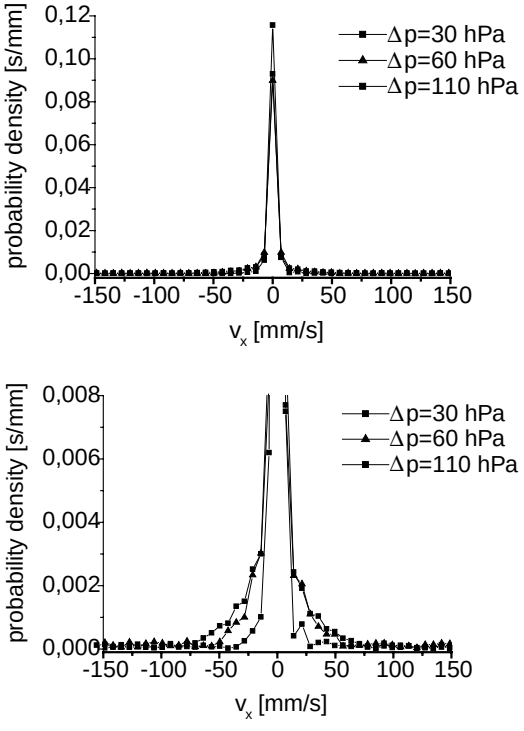

Fig. 4. Propagators in x-direction (horizontal) for different air flow rates, measured on a fluidized poppy seed bed. (Top) full propagator; (bottom) magnification for highlighting the particle fraction with large velocities.

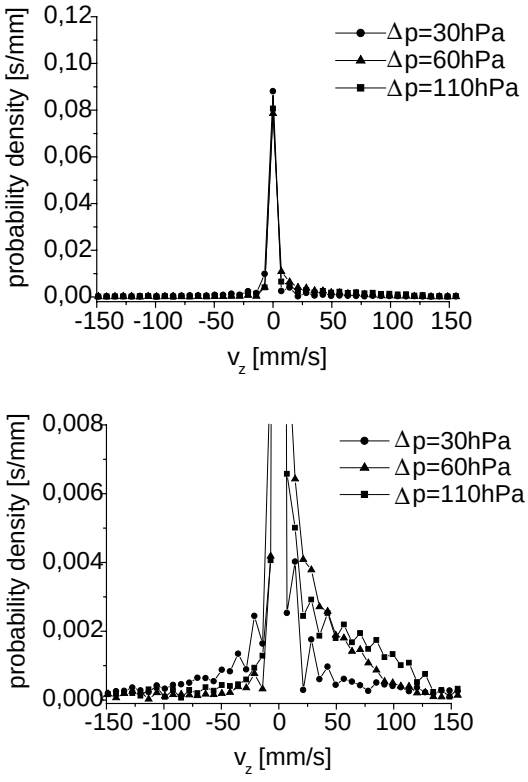

Fig. 5. Propagators in z-direction (vertical) for different air flow rates, measured on a fluidized poppy seed bed. (Top) full propagator; (bottom) magnification for highlighting the particle fraction with large velocities.

as the propagators are dominated by a large peak near zero displacement in all cases. This is in agreement with the visual impression that only a small fraction of the seeds experience significant motion at any time, while the largest part remains mostly static. By increasing the encoding time Δ, the central peak is reduced in intensity (data not shown). The data of Figs. 4 and 5 correspond to the shortest possible value of Δ of 14.5 ms. Although the maximum displacement occurring in the system along x, for instance, is less than one particle diameter for this encoding time, it is still probable that considerable velocity averaging has taken place due to multiple particle collisions during Δ.

For reasons of mass conservation (seeds are not leaving the sensitive volume of the resonator), the average velocity must be vanishing. The mean values of displacements (determined from the first moment of the velocity distribution) are slightly shifted towards positive numbers for the measurements along z, but the average values are within the digital resolution of the experiment. A systematic deviation cannot be excluded completely, but is negligible as far as the qualitative discussion of the results is concerned. Propagators along x show random positive or negative bias of much below the digital resolution.

While the propagators in directions perpendicular to the air flow (x) remain approximately symmetric as one would expect from the lack of any horizontal driving force in the vertically oriented glass cylinder, a pronounced asymmetry appears for the vertical (z) motion. Despite the subjective

impression suggested by Fig. 5 that more particles appear to possess a pronounced upward (positive) velocity, the average displacement of all spins remains zero as has been described above. The balance is maintained by a larger number of particles with rather small negative velocities which are, however, insufficiently resolved in the propagator representation. Interpreting the picture of Werther in a somewhat modified way (see below, Figs. 10 and 12), while particles seem to be moved upward at high speed along with the air stream, they are falling downward with, on average, smaller velocities as they are decelerated by the surrounding bed. This is confirmed with the visual appearance of a fountain-like motion at the top of the bed. As must be the case, the total range of velocities is broadened with increasing air flow rate.

The signal attenuation in a PFG experiment, and quantities derived from it such as the propagator and the dispersion coefficient Eqs. (1)–(6) involve an averaging of displacements over time and ensemble. From the presented data, it cannot be said directly whether the attenuation is dominated by dispersive motion of each single particle, or by the range of different displacements covered by all grains in the sample. The double-encoding experiment first suggested by Callaghan and Manz [49] determines the change of velocities during a mixing time τ. If it is executed in a one-dimensional fashion—i.e., by simultaneously varying two pairs of PFGs, each of them encoding displacement during identical periods Δ—then coherent and incoherent motion can be distinguished from each other. Application of the second gradient pair with opposite polarity to the first one will revert the phase shift accumulated by coherent motion while only velocity changes, i.e., accelerations, lead to a signal decay (“compensated” sequence); repeating the experiment with the same polarity of gradient pairs gives a reference dataset, where signal attenuations of two single PFG experiments add up (“double” sequence). Comparison of both results allows one to estimate the velocity autocorrelation function (VACF) of the system. Compensated sequences have been applied, for instance, for the investigation of Taylor dispersion in Poiseuille flow [50] and to granular flow in a rotating drum [6]. In both cases, the resultant dispersion coefficient is discussed as a function of timescales. In essence, signal attenuations and dispersion coefficients will become identical for the “compensated” and the “double” sequence for mixing times much above a system-specific correlation time τ_c, neglecting velocity changes during the encoding times Δ (see [6] for a detailed discussion). In the system under study, encoding and mixing times are limited by the gradient strength and a determination of the VACF has not yet been achieved.

To highlight the relative contribution of coherent and incoherent motion to dispersion, we compare the signal decay as a function of gradient strength for displacements along x (transverse) in Fig. 6, employing an air pressure drop of 100 hPa. The mixing time τ is defined as the separation between the centers of encoding intervals Δ, where $\Delta = 1.34$ ms.

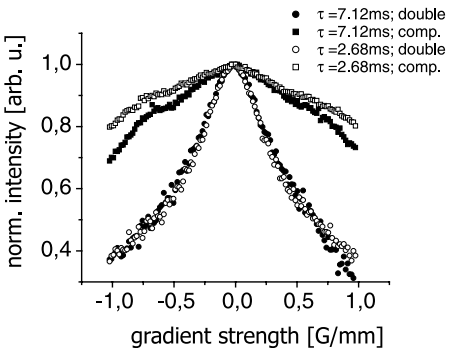

Fig. 6. Signal decay S(g) for the same fluidized poppy seed bed at an air pressure drop of 100 hPa, obtained by a one-dimensional PFG experiment employing two gradient pairs with same (“double”) or opposite sign (“compensated”). $\Delta = 1.34$ ms, and the mixing time is computed between the centers of the two encoding events of duration Δ.

Common to the experiments is a much weaker signal decay as a function of gradient strength when the compensated sequence is applied. The double sequence results in almost undistinguishable decays for both values of τ, while a somewhat weaker decay is observed in the compensated sequence when the mixing time is increased. The dispersion coefficients between both sequences differ by about a factor of 3–4. The signal decay of the compensated sequence is related to the “true” dispersion due to particle collisions, since ballistic flight paths can be assumed between collisions. However, it is important to note that the collision time does not have to be equal to the correlation time. For instance, a granular particle following the motion of a gas bubble will collide with its neighbors but maintain its general direction of motion. The actual correlation time of the granular system can only be estimated as being significantly longer than the longest mixing time of 7.1 ms. It is worth noting that a much less pronounced difference between both experiments was observed for the z (vertical) component of motion, where velocity changes seem to appear on a shorter timescale.

In a recent publication, the strategy of multiple PFGs [51] was applied to a different gas-fluidized granular medium [19,20]; in this case, correlation times below 1 ms were found and the results were interpreted in terms of grain caging and hopping between cages. We are currently conducting further studies to verify whether similar conclusions can be drawn for the poppy seed bed in the bubbling phase investigated in this work.

4.2. Dispersion coefficients

In Fig. 7, the signal decays as a function of gradient strength are shown for motion along z and for different air flow rates. The results represent the raw data of the propagators discussed above, and are shown in the conventional plot of $\ln S$ vs. $\mathbf{q}^2$, which allows the determination of the dispersion coefficient according to Eq. (6). A Gaussian propagator would result in a straight line. In contrast, strongly curved decay functions are found, which indicate

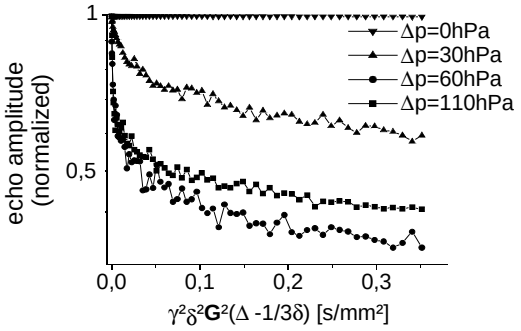

Fig. 7. Plot of ln S vs. $\mathbf{q}^2$ (motion in z-direction).

Table 1
Compilation of the obtained dispersion coefficients in x- and z-directions

Δp (hPa)	30	60	110
D_{eff} (10^{-6}m^2/s) in x	1.90	13.7	24.7
D_{eff} (10^{-6}m^2/s) in z	9.28	52.9	62.8
Ratio D_{eff}, z/x	4.9	3.9	2.5

The mean error of all dispersion coefficients is around 15%.

that much more complex motion is present in the system. The shallower decay at higher $\mathbf{q}$ values corresponds to "slow" particles, i.e., those which represent the pronounced peak near zero displacement in Figs. 4 and 5.

The dispersion coefficients derived from the initial slope of the decay function are listed in Table 1. They show a pronounced dependence on gas flow rate. The essential information of these measurements, however, is the ratio between dispersion coefficients along z and x, respectively, which can be directly compared. The ratio is decreasing with larger air flow rate. This can be related to the observation that with increasing air pressure drop, more and more particles take part in the process of internal motion, so that strong dispersion parallel as well as perpendicular to the air stream direction takes place at the same time. This assumption coincides with the finding that in the propagators, the relative weight of the peak near zero displacement decreases with increasing air flow rate. However, resolving the velocity pattern directly by combination with MRI can provide a much stronger support to this concept.

4.3. Velocity imaging and vector plots

Fig. 8 shows two velocity encoded images, which were obtained from 5 mm thick slices inside a bed of poppy seeds. Fig. 8A depicts the velocities of the slice from the upper part of the bed, Fig. 8B from the lower slice, the distance of these two slices being 10 mm. The scale is represented by the color bar. The bed height in the absence of air flow is 2.7 cm. For the chosen air flow rate of 70 hPa, the average height increases to 3.5 cm, so the slices represent generally the upper and the lower part of the fluidized bed (see sketch in Fig. 10).

In both images, one finds predominantly positive (upward) velocities in the center of the bed, while negative values are dominating at the edge, i.e., near the inner wall

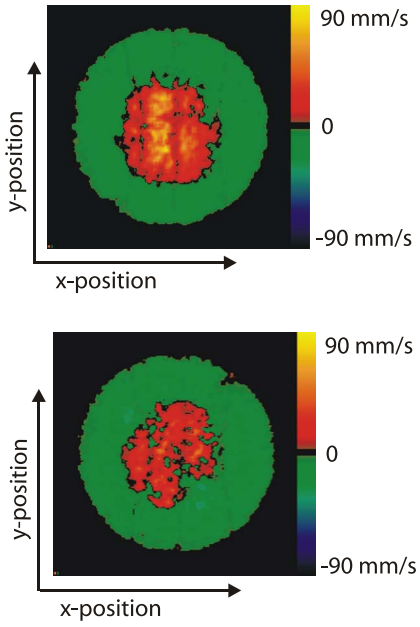

Fig. 8. Velocity images of 5 mm slices taken from (top) the upper and (bottom) the lower part of a 2.7 cm high fluidized poppy seed bed inside a glass vessel; the distance between the slices is 10 mm. The color bar represents the particle velocity in the bed (vertical stripes are data processing artifacts). Phase values outside the glass vessel have been set to zero.

of the glass cylinder. The averaged maximum positive velocity, which, in this case, is the velocity with the gas stream, is higher for the upper slice compared to the lower slice, as can be seen more easily in the 3D surface plots of the same data (Fig. 9). The average velocity, which is required to be zero to ensure the particle flux balance, was determined as −2.5 mm/s (top slice) and −7 mm/s (bottom slice). As the reason for this deviation, a systematic trend cannot be ruled out completely, e.g., by velocity averaging during the encoding time. The general observation that higher positive (upward) than negative (downward) velocities do occur is in agreement with the results of the propagator measurements discussed above Fig. 10 summarizes these findings in a simplified plot following Werther's model (Fig. 2B), where higher velocities in the center are indicated by a longer arrow.

For the behavior of upward moving seeds, the explanation is quite straightforward. Because of the higher resistance of the particles in the lower part of the fluidized bed due to interparticle friction, the velocity is smaller than for the particles in the upper region. Particles in the upper slice can move almost freely and feature a fountain-like pattern, which can easily be seen by the naked eye; they thus attain maximum upward velocities near the top layer where the particle density is being reduced.

The downwards movement of the seeds is limited by the boundary at the bottom of the bed, and also by the interactions with the surrounding particles of the packing and the glass wall. In both slices, which have sufficient distance from the bottom layer, the maximum negative velocity is found to be similar (see the 3D surface plots in Fig. 9).

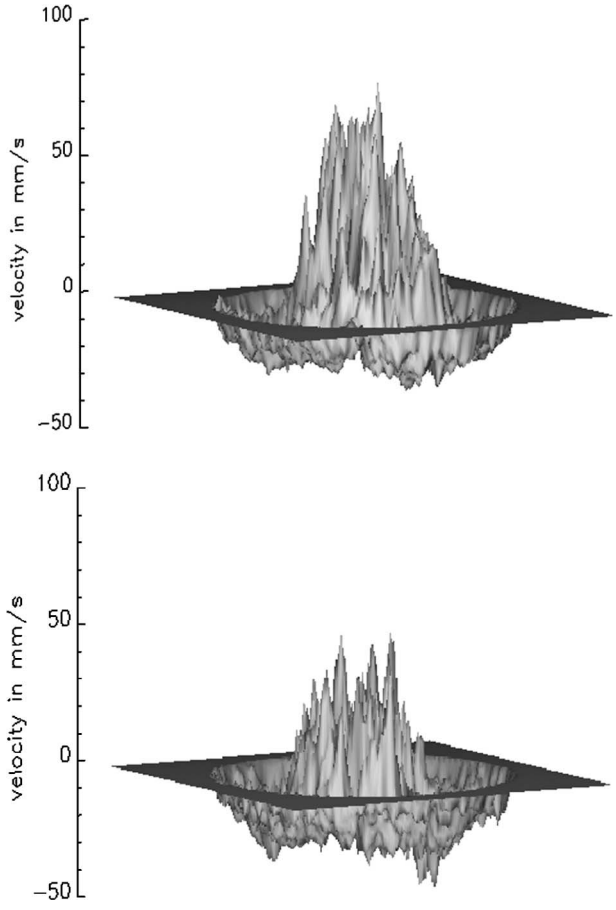

Fig. 9. 3D surface plots of the velocity imaging data; (top) the upper and (bottom) the lower part of a 2.7 cm high fluidized poppy seed bed inside a glass vessel (same data as Fig. 8). Phase values outside the glass vessel have been set to zero.

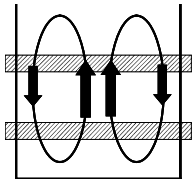

Fig. 10. Model for the upward and downward movement of the seeds inside the fluidized bed, distinguishing between the upper and lower region where velocity imaging experiments have been carried out.

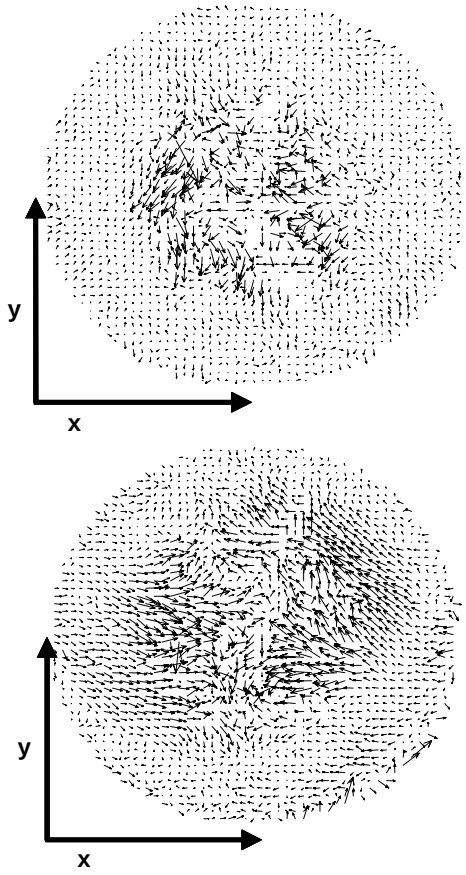

Fig. 11. Vector plots of transverse particle velocities. (Top) upper part of the bed; (bottom) lower part of the bed.

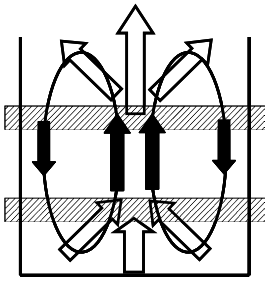

Fig. 12. Schematic of the particle motion inside the fluidized bed, especially the transverse part. The bottom slice was more influenced by the inwards movement, the top slice by the outward movement.

To also visualize the transverse velocity pattern, imaging experiments with encodings along x and y were combined to generate vector plots, the results of which are shown in Fig. 11. These plots represent the velocities in the same slices as discussed above for the z component of motion (Figs. 8 and 9). The length of the arrows is proportional to the velocity, so that one can distinguish between areas of higher and lower particle velocity. As only a few particles contribute to the signal in each voxel at any given event of signal acquisition, the averaging needs to be taken over a larger number of accumulations than is experimentally feasible. Nevertheless, an average pattern is revealed from the velocity plots despite the presence of substantial fluctuations. What can be said with certainty is that in general, larger transverse velocities do appear in the center region of the slices and in particular in the lower region of the bed. A tendency of particle motion from the outside toward the center of the bed is visible for the bottom slice. This can be understood by looking at the schematic of Werther's model, which we now have supplemented by the transverse components of motion (Fig. 12). From the boundary conditions, it becomes clear that motion inside the single cell-pattern predominantly takes place inwards in the bottom part but outwards in the top part of the granular bed.

The outward motion in the upper slice (Fig. 11, top), however, is not well defined in the experimental results, possibly a consequence of larger velocity fluctuations in the top region near the open surface, compared to the slice near the bottom of the bed.

Combining the findings of the different velocity encoded images, one can summarize that in the upper region of the bed, larger upward but smaller horizontal velocities occur, while the bottom region is characterized by smaller upward and higher transverse velocities. This behavior becomes most evident around the central axis of the bed where spout-like motion is expected to be dominating. This suspected negative correlation between vertical and horizontal velocities might be quantifiable by applying suitable two-dimensional propagator techniques that measure velocities in orthogonal directions simultaneously [52].

5. Conclusion

In summary, all measurements conform with the model introduced by Werther. For fluidized beds with small diameter and comparatively large particles, the inner particles follow an upwards movement and the outer particles a downwards movement, which could be revealed by 2D velocity images. A second cell of particle motion, which has sometimes been reported either next to or above the main cell, was not observed for the small system under study. From these images it could also be concluded that the magnitude of upward motion has a tendency to increase toward the upper (open) surface of the granular bed, while the downward motion did not show such a pronounced evolution. Averaging over the motion in the whole bed provides a measure of direction-dependent dispersion coefficients; in particular, the ratio between dispersion coefficients along vertical and horizontal directions was found to decrease with larger air flow rate.

This study has demonstrated the feasibility to conduct velocity imaging experiments on random motion of granular beds with small particle numbers. Higher-dimensional experiments are possible in principle, but the necessary averaging does require the use of a larger number of particles, i.e., larger cells or smaller grains, which will also make the system more comparable to technical applications. Changing the dimensions of the granular bed, and at the same time the grain material—the most important property of which is to provide an NMR signal of sufficient lifetime to allow imaging and velocity encoding with an appropriate evolution time—will also make accessible the different regimes of granular behavior, in particular as the dynamics in the vicinity of the granular phase transitions is concerned. Ongoing research will focus on the fundamental questions of granular systems but maintain technical relevance due to the wide range of industrial applications of fluidized beds.

Acknowledgments

This work has been supported in part by Deutsche Forschungsgemeinschaft DFG (Bl 231/25). We are grateful to M. Küppers for assistance in the course of the experimental work and excellent help, solving data processing problems.

References

[1] J. Duran, Sands, Powders, and Grains—An Introduction to the Physics of Granular Materials, Springer, New York, 2000.
[2] D. Bideau, J. Dodds (Eds.), Physics of Granular Media, Les Houches Series, Nova Science Publishers, New York, 1991.
[3] R.L. Brown, J.C. Richards, Principles of Powder Mechanics, Pergamon Press, Oxford, 1970.
[4] D. Geldart, Types of gas fluidization, Powder Technology 7 (1973) 258.
[5] M. Ghadiri, Gas and particle flow patterns in fluidised beds, in: D. Bideau, J. Dodds (Eds.), Physics of Granular Media, Les Houches series, Nova Science Publishers, Cambridge, 1991.
[6] A. Caprihan, J.D. Seymour, Correlation time and diffusion coefficient imaging: application to a granular flow system, J. Magn. Reson. 144 (2000) 96.
[7] J.D. Seymour, A. Caprihan, S.A. Altobelli, E. Fukushima, Pulsed gradient spin echo nuclear magnetic resonance imaging of diffusion in granular flow, Phys. Rev. Lett. 84 (2000) 266.
[8] K. Yamane, M. Nakagawa, S.A. Altobelli, T. Tanaka, Y. Tsuji, Steady particulate flows in a horizontal rotating cylinder, Phys. Fluids 10 (1998) 1419.
[9] M. Nakagawa, S.A. Altobelli, A. Caprihan, E. Fukushima, An MRI study: axial migration of radially segregated core of granular mixture in a horizontal rotating cylinder, Chem. Eng. Sci. 52 (1997) 4423.
[10] K.M. Hill, A. Caprihan, J. Kakalios, Bulk segregation in rotated granular material measured by magnetic resonance imaging, Phys. Rev. Lett. 78 (1996) 50.
[11] D.M. Mueth, Measurements of particle dynamics in slow, dense granular Couette flow, Phys. Rev. E 67 (2003) 011304.
[12] P. Porion, N. Sommier, A.-M. Faugère, P. Evesque, Dynamics of size segregation and mixing of granular materials in a 3D-blender by NMR imaging investigation, Power Technol. 141 (2004) 55.
[13] X. Yang, D. Candela, Potential energy in a three-dimensional vibrated granular medium measured by NMR imaging, Phys. Rev. Lett. 85 (2000) 298.
[14] X. Yuan, C. Huan, D. Candela, R.W. Mair, R.L. Walsworth, Measurements of grain motion in a dense, three-dimensional granular fluid, Phys. Rev. Lett. 88 (2002) 044301.
[15] C. Huan, X. Yang, D. Candela, NMR experiments on a three-dimensional vibrofluidized granular medium, Phys. Rev. E 69 (2004) 041302.
[16] E.E. Ehrichs, H.M. Jaeger, G.S. Karczmar, J.B. Knight, V.Y. Kuperman, S.R. Nagel, Granular convection observed by magnetic resonance imaging, Science 267 (1995) 1632.
[17] J.B. Knight, E.E. Ehrichs, V.Y. Kuperman, J.K. Flint, H.M. Jaeger, S.R. Nagel, Experimental study of granular convection, Phys. Rev. E 54 (1996) 5726.
[18] A. Caprihan, E. Fukushima, A.D. Rosato, M. Kos, Magnetic resonance imaging of vibrating granular beds by spatial scanning, Rev. Sci. Instrum. 68 (1997) 4217.
[19] J. Stepisnik, S. Lasic, A. Mohoric, I. Sersa, G. Planinsic, Autocorrelation spectra of air-fluidized granular systems by the NMR spin echo, in: Garcia-Rojo, Herrmann, McNamara (Eds.), Powders and Grains, Taylor & Francis, London, 2005.
[20] J. Stepisnik, S. Lasic, I. Sersa, A.Mohoric, G. Planinsic, Dynamics of air-fluidized granular system measured by the modulated gradient spin-echo, Available from <arXiv:physics/0505214>.
[21] E. Fukushima, Granular flow studies by NMR: a chronology, Adv. Comp. Sys. 4 (2001) 503.

[22] E. Fukushima, NMR imaging in chemical engineering, in: S. Stapf, S. Han (Eds.), Granular Flow, VCH-Wiley, Weinheim, 2005.
[23] J.F. Davidson, R. Clift, D. Harrison (Eds.), Fluidization, second ed., Academic Press, London, 1985.
[24] D. Geldart, Fluidised bed as a chemical reactor—a critical review of first 25 years, Chem. Ind. 35 (1967) 1474.
[25] L. Oger, Analysis of the geometry of granular media, in: J. Dodds (Ed.), Physics of Granular Media, Les Houches Series, Nova Science Publishers, New York, 1991.
[26] J. Werther, Influence of the bed diameter on the hydrodynamics of gas-fluidized beds, AIChE Symp. Ser. No. 141, vol. 70, 1974, p. 53.
[27] J. Werther, Strömungsmechanische Grundlagen der Wirbelschichttechnik, Chem. Eng. Technol. 49 (1977) 193.
[28] L. Reh, Strömungs- und Austauschverhalten von Wirbelschichten, Chem. Eng. Tech. 46 (1974) 180.
[29] J.M. Valverde, A. Castellanos, P. Mills, M.A.S. Quintanilla, Effect of particle size and interparticle force on the fluidization behaviour of gas-fluidized beds, Phys. Rev. E 67 (2003) 051305.
[30] J.M. Valverde, A. Castellanos, M.A.S. Quintanilla, Self-diffusion in a gas-fluidized bed of fine powder, Phys. Rev. Lett. 86 (2001) 3020.
[31] N. Menon, D.J. Durian, Particle motions in a gas-fluidized bed of sand, Phys. Rev. Lett. 79 (1997) 3407.
[32] K. Ichiki, H. Hayakawa, Dynamical simulation of fluidized beds: hydrodynamically interacting granular particles, Phys. Rev. E 52 (1995) 658.
[33] K. Ichiki, H. Hayakawa, Analysis of statistical quantities in simulation of fluidized beds, Phys. Rev. E 57 (1998) 1990.
[34] R. Soto, M. Mareschal, Departure from Fourier's law for fluidized granular media, Phys. Rev. Lett. 83 (1999) 5003.
[35] M.J.V. Goldschmidt, R. Beetstra, J.A.M. Kuipers, Hydrodynamic modelling of dense gas-fluidised beds: comparison of the kinetic theory of granular flow with 3D hard-sphere discrete particle simulations, Chem. Eng. Sci. 57 (2002) 2059.
[36] P.S. Fennell et al., A study of the mixing of solids in gas-fluidized beds using ultra-fast MRI, Chem. Eng. Sci. 60 (2005) 2085.
[37] R. Wang, M.S. Rosen, D. Candela, R.W. Mair, R.L. Walsworth, Study of gas-fluidization dynamics with laser-polarized ^{129}Xe, Chem. Eng. Technol. 23 (2005) 203.
[38] R. Savelsberg, D.E. Demco, B. Blümich, S. Stapf, Particle motion in gas-fluidized granular systems by pulsed-field gradient nuclear magnetic resonance, Phys. Rev. E 65 (2002) 020301.
[39] Y. Wu, D. Gidaspow, Hydrodynamic simulation of methanol synthesis in gas-liquid slurry bubble column reactors, Chem. Eng. Sci. 55 (2000) 573.
[40] J.D. Wang, Y.R. Yang, W.J. Shu, L.X. Hou, A Study of the flow pattern of multi-zone in fluidised bed polymerisation, AIChE J (submitted).
[41] D. Kunii, O. Levenspiel, Fluidization Engineering, Butterworth-Heinemann, Boston, 1991.
[42] K. Winnaker, L. Küchler, Chemische Technik—Prozesse und Produkte, Band 1: Methodische Grundlagen, 5. Auflage, Wiley-VCH, Weinheim, 2004.
[43] L. Reh, Auswahlkriterien für nichtkatalytische Gas/Feststoff-Hochtemperaturreaktoren, Chem. Eng. Technol. 49 (1977) 786.
[44] K.B. Mathur, Chapter 17: Spouted beds, in: J.F. Davidson, D. Harrison (Eds.), Fluidization, Academic Press, New York, 1971.
[45] J. Kärger, W. Heink, The propagator representation of molecular transport in microporous crystallites, J. Magn. Reson. 51 (1983) 1.
[46] E.O. Stejskal, J.E. Tanner, Spin diffusion measurements: spin echos in the presence of a time-dependent field gradient, J. Chem. Phys. 42 (1965) 288.
[47] P.T. Callaghan, Principles of Nuclear Magnetic Resonance Microscopy, Clarendon Press, Oxford, 1991.
[48] M. Sommerfeld, Analysis of collision effects for turbulent gas-particle flow in a horizontal channel: Part I. particle transport, Int. J. Multiphase Flow 29 (2003) 675.
[49] P.T. Callaghan, B. Manz, Velocity exchange spectroscopy, J. Magn. Reson. A 106 (1994) 260.
[50] S.L. Codd, B. Manz, J.E. Seymour, P.T. Callaghan, Taylor dispersion and molecular displacement in Poiseuille flow, Phys. Rev. E 60 (1999) 3491.
[51] P.T. Callaghan, J. Stepisnik, Frequency-domain analysis of spin motion using modulated gradient NMR, J. Magn. Reson. A 117 (1995) 118.
[52] S. Stapf, K.J. Packer, R.G. Graham, J.-F. Thovert, P.M. Adler, Spatial correlations and dispersion for fluid transport through packed glass beads, Phys. Rev. E 58 (1998) 6206.